

Brushes of semiflexible polymers in equilibrium and under flow in super-hydrophobic regime

K. Speyer*[†], C. Pastorino*[†]

**Departamento de Física de la Materia Condensada, Centro Atómico Constituyentes, CNEA, Av.Gral. Paz 1499, 1650 Pcia. de Buenos Aires, Argentina* and*

† CONICET, Avenida Rivadavia 1917, C1033AAJ Buenos Aires, Argentina

We performed molecular dynamics simulations to study equilibrium and flow properties of a liquid in a nano-channel with confining surfaces coated with a layer of grafted semiflexible polymers. The coverage spans a wide range of grafting densities from essentially isolated chains to dense brushes. The end-grafted polymers were described by a bead spring model with an harmonic potential to include the bond stiffness of the chains. We varied the rigidity of the chains, from fully flexible polymers to rigid rods, in which the configurational entropy of the chains is negligible. The brush-liquid interaction was tuned to obtain a super-hydrophobic channel, in which the liquid did not penetrate the polymer brush, giving rise to a Cassie-Baxter state. Equilibrium properties such as brush height and bending energy were measured, varying the grafting density and the stiffness of the polymers. We studied also the characteristics of the brush-liquid interface and the morphology of the polymers chains supporting the liquid for different bending rigidities. Non-equilibrium simulations were performed, moving the walls of the channel in opposite directions at constant speed, obtaining a Couette velocity profile in the bulk liquid. The molecular degrees of freedom of the polymers were studied as a function of the Weissenberg number. Also, the violation of the no-slip boundary condition and the slip properties were analyzed as a function of the shear rate, grafting density and bending stiffness. At high grafting densities, a finite slip length independent of the shear rate or bending constant was found, while at low grafting densities a very interesting non-monotonic behaviour on the bending constant is observed.

I. INTRODUCTION

Polymer brushes are enormously versatile systems, whose properties can be tailored chemically and physically[1–3]. They were studied with great interest due to their technological significance, biophysical importance and theoretical subtleties and complexity. They find important applications in colloid stabilization, lubrication, and developments where friction[4], adhesion and wetting properties are important[1]. They are also used as coatings in “smart surfaces” to fine tune reversibly some property of an interface upon changes in external stimuli, for example, PH[5], temperature, solvent quality[6, 7]. Brushes are at the forefront of recent developments, ranging from responsive bio-interphases, controlled drug-delivery and release systems, thin films and particles, which act as sensors of minute amounts of analytes[3, 6]. The geometry and curvature of the grafted surface contribute also to distinctive properties of brushes, which can be grown in planar or cylindrical geometries, in the surface of nanoparticles or into the backbone of macromolecules (bottle-brushes)[1, 8]. An important biophysical system of end-grafted semiflexible polymers is the endothelial glycocalyx layer, present in the inner side of vasculature in animals and plants[9]. It has a complex structure formed by a matrix of macromolecular carbohydrates, consisting of proteoglycans and glycoproteins, that coat the surface of endothelial cells[9, 10].

It is known to have important functions as modulator of permeability in the exchange of water, primary molecular sieve of plasma proteins, mechanotransducer of fluid shear stress and as regulator of red and white blood cells[9]. From a mesoscopic point of view, this branched comb-like polymer brush, can be modelled as composed of semiflexible homopolymer chains whose beads have the size of the side-chains[10]. In this model, the glycocalyx is closely related to the geometry we study in this work.

Polymer brushes were studied intensely in equilibrium and non-equilibrium conditions[8, 11, 12] by computer simulations and theory[13]. However, the vast majority of work was devoted to fully flexible polymer chains. Computer simulation of coarse-grained systems studied friction of bearing brushes [14–17] and the flow of simple liquids or polymer melts confined in brush-coated polymer channels as function of grafting density, interface properties and flow intensity[18–22]. Milchev and Binder studied the structure of brushes formed by semiflexible chains by Monte Carlo and molecular dynamics simulations[23]. They found an interesting phase transition of the system under compression, which presents buckling at moderate pressures and bending at higher pressures[24]. The first bonds of the grafted polymers, in this reference, are directed perpendicularly to the grafting plane, as it is the case in our work. Using soft potentials within the Dissipative Particle Dynamics (DPD) simulation scheme various groups studied different aspects of a polymer brush exposed to flow[10, 21, 25]. Deng *et al.*[10] included bending rigidity in their model to account for semiflexible polymers in the context of glycocalyx and studied brush height and slip length for

*Electronic address: pastor@cnea.gov.ar

Couette (shear-driven) and Poiseuille (pressure-driven) flows. Benetatos *et al.* explored the morphology and in-plane collapse of a grafted layer of attractive semiflexible chains, analysing the bundling of neighboring chains[26]. Kim *et al* studied the height behavior of the brush layer as function of chain stiffness, shear rate and grafting density by Brownian hydrodynamics, lattice Boltzmann simulations and mean field theories[27]. More recently, Römer and Fedosov[28] developed a theoretical model and compared with DPD simulations, a brush of stiff polymers under flow. They found a good agreement of model and simulations for brush height, velocity profile and apparent flow viscosity, for a wide range of shear rates and grafting densities. Active semiflexible polymers (filaments) have been studied to analyse efficiency of pumping of liquid[29] and methachronal waves in bidimensional arrays of grafted chains[30]. In these works the focus is in the hydrodynamic coupling of the semiflexible chains and its role in transport efficiency.

Relevant to the present work are also the superhydrophobic surfaces. In these, surface texture or structure at the micro and/or nanoscopic level, is used to enhance the intrinsic hydrophobic chemistry of the surface, to produce highly non-wetting surfaces. Superhydrophobic surfaces typically exhibit very high water-repellency, which translates in high contact angles Θ of droplets deposited over them ($\Theta > 150^\circ$). This property is desirable for an important range of technological applications, such as self-cleaning surfaces, anti-fog, anti-corrosion, icephobicity and fluidic drag reduction[31, 32]. Polymer brushes and coatings are also a way to obtain super-hydrophobic surfaces[5, 33]. In recent years, new methodologies were developed to produce specific super-hydrophobic surfaces on small and large scales, suitable for basic research and production, respectively. Despite this, the underlying basic mechanisms of the super-hydrophobic effects are under discussion, beyond the basics developed a long time ago by Wenzel, Cassie and Baxter[34, 35]. This includes, for example, the role of roughness at multiple scales, which has also importance in the development of bio-mimetic surfaces, whose biological counterparts, such as the lotus leaf, are still under active research[36]. Mimicking nature, is a promising route to the developing of multifunctional super-hydrophobic surfaces. Lotus leaf's morphology, for example, was used to produce self-cleaning films and iridescent super-hydrophobic surfaces were developed to obtain anisotropic wettability by copying the structure of butterfly wings[32].

Experimental results confirm the efficiency of superhydrophobic coatings to reduce the drag of objects moving in water[37, 38] or, equivalently, increase the flow rate of liquid flowing in channels[39, 40]. The friction reduction is attributed to the air filling of local structure in the solid-gas composite interfaces, which gives rise to surface slip[32, 41–43].

In this work, we study in equilibrium and under flow, the interface of a liquid and a layer of end-grafted semiflexible polymers for different bending rigidities and as

a function of grafting density. The interaction between grafted chains and liquid is chosen such that the interface is hydrophobic and compatible with super-hydrophobic behavior, for a wide range of grafting densities. A typical snapshot of the system in the superhydrophobic Cassie-Baxter state, for the stiffest polymers considered in this work, can be observed in Fig. 1. We studied a small number of bending rigidities, ranging from fully flexible to highly stiff polymers, such that the polymer resembles a pillar, typical of superhydrophobic surfaces, and its configurational entropy is minimal. This implies also statistical Kuhn segments much smaller, of the order, or much higher than the contour length of the chains. In section II we present the simulation technique, details of the model, and the way in which we imposed flow in the system. Simulation results are presented in section III, devoting subsections III A and III B to equilibrium properties and behavior under flow, respectively. We provide a final discussion and conclusions in Section IV.

II. MODEL AND SIMULATION TECHNIQUES

The polymer chains are simulated by the widely utilized coarse-grained bead-spring Kremer-Grest model[44, 45]. A finite extensible nonlinear elastic (FENE) potential models the bond interactions between neighboring beads of the same chain.

$$U_{FENE} = \begin{cases} -\frac{1}{2}kR_0^2 \ln \left[1 - \left(\frac{r}{R_0} \right)^2 \right], & r < R_0 \\ \infty, & r \geq R_0 \end{cases}, \quad (1)$$

where $R_0 = 1.5\sigma$, the spring constant $k = 30\varepsilon/\sigma^2$, and $r = |\mathbf{r}_i - \mathbf{r}_j|$ is the distance between neighboring monomers. This potential simulates the correct dynamics of polymers for a variety of thermodynamic conditions[44, 45]. All monomers of the $N = 10$ polymer chains we simulated, interact with each other through a truncated and shifted Lennard-Jones potential

$$U_{INT} = \begin{cases} U_{LJ}(r) - U_{LJ}(r_C), & r < r_C \\ 0, & r \geq r_C \end{cases} \quad (2)$$

with U_{LJ} is the standard Lennard-Jones potential:

$$U_{LJ} = 4\varepsilon_{ab} \left[\left(\frac{\sigma}{r} \right)^{12} - \left(\frac{\sigma}{r} \right)^6 \right], \quad (3)$$

where $\sigma = 1$ defines the length unit. r_C is the interaction cut-off radius: if the distance between particles exceeds r_C , this interaction is turned off. For the interaction between particles belonging to the polymer, the cut-off radius was set to the minimum of the Lennard-Jones potential $r_C = \sqrt[6]{2}\sigma \simeq 1.12\sigma$, giving a purely repulsive force which is interpreted as a polymer in good solvent conditions. For the liquid-liquid and liquid-polymer interactions, the cut-off radius was set to twice the minimum of the potential $r_C = 2\sqrt[6]{2}\sigma \simeq 2.24\sigma$, to include

attractive interactions. This allows the formation of liquid and gas phases for temperatures below the evaporating point. The interaction strength ε_{ab} was set to unity for the polymer-polymer and liquid-liquid interactions $\varepsilon_{pp} = \varepsilon_{ll} \equiv \varepsilon = 1$, and defines the energy unit. The temperature unit is therefore ε/k_B . For polymer-liquid interactions the parameter was set to $\varepsilon_{pl} = 1/3\varepsilon$, representing the chemical incompatibility between species. Rough surfaces with similar interaction potential and ε_{pl} parameter have been studied previously[46–49], resulting in highly hydrophobic substrates and yielding to contact angles $\theta \sim 120^\circ$ for droplets deposited over that surfaces.

The rigidity of the polymers is imposed by a harmonic potential

$$U_b(\mathbf{r}_i, \mathbf{r}_{i+1}, \mathbf{r}_{i+2}) = \frac{1}{2}k_b\theta_{i,i+1,i+2}^2, \quad (4)$$

where $\theta_{i,i+1,i+2}$ is the angle formed by two consecutive bonds, and is measured from the polymer backbone. The bending constant k_b is one of the parameters varied in this work to explore different persistence lengths. It is important to note that the sum of bending forces over all the beads is null, so the forces applied on the free end bead are transmitted, in average, to the grafted bead. To induce a privileged orientation of the polymer chains perpendicular to the substrate, the bending force calculations are performed adding a phantom bead exactly below the fixed end. This additional bond generates a force on the second bead, favouring an orientation angle $\theta_1 = 90^\circ$ with respect to the wall.

The walls at $z = 0$ and $z = D$ were modelled as impenetrable flat surfaces, which interact with monomers via a purely repulsive integrated Lennard-Jones potential of the form

$$U_{wall}(z) = |A| \left(\frac{\sigma}{r}\right)^9 + A \left(\frac{\sigma}{r}\right)^3, \quad (5)$$

with $A = 3.2\varepsilon$ [19, 22].

The grafted end-beads of the 10-bead polymers are placed at a distance $z = 1.2\sigma$ from the substrate, and the lateral positions is randomly chosen. The number of grafted sites is determined by the grafting density. The initial positions of the liquid particles are uniformly random distributed, and a force switch-on mechanism is used to relax the system towards thermodynamic equilibrium and eliminate the overlap between beads. Production runs of typically 10^7 steps are done after this relaxation and 10^6 time steps of thermalization.

We used the dissipative particle dynamics (DPD) scheme[50, 51] to perform the simulations at constant temperature. An important feature of this thermostat is that it accounts for correct hydrodynamic behaviour[52], which is essential to obtain reliable results out of equilibrium[53–55]. The equation of motion for a particle reads:

$$m \frac{d^2 \mathbf{r}_i}{dt^2} = \mathbf{F}_i + \mathbf{F}_i^D + \mathbf{F}_i^R, \quad (6)$$

where \mathbf{F}_i represents the conservative forces, \mathbf{F}_i^D and \mathbf{F}_i^R are the dissipative and the random forces, respectively. The mass m is set to unity for all particles. Random and dissipative forces are applied in pairs, in such a way that local momentum is conserved. The form for these forces is

$$\mathbf{F}_i^D = \sum_{j \neq i} \mathbf{F}_{ij}^D, \quad \mathbf{F}_{ij}^D = -\gamma \omega^D(r_{ij})(\hat{\mathbf{r}}_{ij} \cdot \mathbf{v}_{ij}) \hat{\mathbf{r}}_{ij}, \quad (7)$$

$$\mathbf{F}_i^R = \sum_{j \neq i} \mathbf{F}_{ij}^R, \quad \mathbf{F}_{ij}^R = \zeta \omega^R(r_{ij}) \eta_{ij} \hat{\mathbf{r}}_{ij}, \quad (8)$$

where the notation $\mathbf{a}_{ij} = \mathbf{a}_i - \mathbf{a}_j$ is used for vectors, γ is the friction constant, ζ denotes the noise strength, ω^D and ω^R are weight functions. These parameters and functions are not completely free to choose in order to satisfy the fluctuation-dissipation theorem. This constrain impose the conditions $\zeta^2 = 2k_B T \gamma$, and $[\omega^R]^2 = \omega^D$. The parameter γ was set to unity in all simulations, because this value allows to maintain constant temperature and doesn't produce a significative over-damping of conservative forces[55]. The random variable η_{ij} has zero mean and second moment $\langle \eta_{ij}(t) \eta_{kl}(t') \rangle = \delta_{ik} \delta_{jl} \delta(t - t')$. The usual choice of the weight functions for continuous forces was made[53, 55].

$$[\omega^R]^2 = \omega^D = \begin{cases} (1 - r/r_C)^2, & r < r_C \\ 0, & r \geq r_C \end{cases}, \quad (9)$$

where the cut-off radius is chosen equal to that of Lennard-Jones interaction: $r_C = 2\sqrt[6]{2}\sigma \simeq 2.24\sigma$.

We define the time units in terms of the Lennard-Jones parameters and the mass $\tau \equiv \sigma \sqrt{m/\varepsilon}$. The Velocity Verlet[56] integration scheme was used to integrate the equations of motion 6, with time steps in the range $2 \cdot 10^{-4} \tau \leq dt \leq 5 \cdot 10^{-4} \tau$. Under these conditions, it was possible to perform equilibrium and non-equilibrium simulations, maintaining a constant temperature over the whole system. We tested this with temperature profiles across the channel, obtained from the mean square velocity of the particles.

The temperature value $T = 0.8\varepsilon/k_B$ was chosen to set the liquid far enough from the condensation point and to have a relatively low vapor density[57]. In thermal equilibrium, the liquid and gas number densities are $\rho_l = 0.69\sigma^{-3}$ and $\rho_v = 0.03\sigma^{-3}$, respectively. Several systems were studied, varying the number of grafted chains per surface area and bending constant. In order to compare quantitatively the behaviour of the different systems, it is necessary to maintain some magnitude constant for all cases. We chose to maintain the liquid density in the bulk equal in all studied systems to provide a consistent thermodynamic condition. Therefore, the number of liquid particles was changed so that in every equilibrated system, the bulk liquid density satisfied

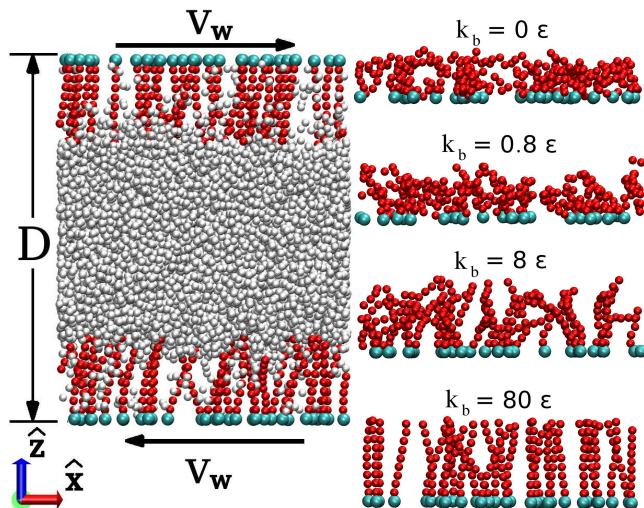


Figure 1: Left panel: Snapshot of the simulated system for a grafting density of $\rho_g = 0.05\sigma^{-2}$ and bending constant $k_b = 80\epsilon$ in equilibrium. Particles of the liquid are shown in light gray, the polymer chains in the brush are presented in red, while their end beads (steadily fixed to the wall) are shown in light-blue. Right panel: Configuration of the polymer brushes for the different bending rigidities studied (the liquid is not shown).

$0.693\sigma^{-3} \leq \rho_l \leq 0.697\sigma^{-3}$. The low tolerance implemented is due to the fact that the normal pressure is a rapidly varying function of ρ_l . This means that the total number of liquid particles compatible with the range of allowed densities may vary in about ~ 300 , which constitutes roughly 3% of the total number of liquid particles in a typical system.

The grafting density ρ_g is defined as the number of grafted chains per unit area. Several systems with ρ_g ranging from $0.02\sigma^{-2}$ to $0.6\sigma^{-2}$ were studied. These values of grafting density correspond to a mean distance between grafting sites $l = 7.1\sigma$ and $l = 1.3\sigma$, respectively. Taking into account that the contour length of the polymers is $l_c \simeq 8.5\sigma$ ($R_{end} \simeq 4.5\sigma$ for fully flexible isolated chains), the range of ρ_g selected allows to study regimes from single chain condition, or the so-called mushroom regime for flexible polymers, to a dense brush case. The distance between walls is $D = 40\sigma$ (see Fig. 1), and the lateral dimensions of the simulation box are $L_x = 30\sigma$ and $L_y = 20\sigma$.

Out of equilibrium simulations were produced by moving the walls at constant velocity and in opposite directions. The polymers moving with the wall drag the liquid and give place to a linear velocity profile in the bulk of the liquid. The velocity of the walls was varied from $v_W = 0$ to $v_W = 1.0\sigma/\tau$, which correspond to shear rates between $\dot{\gamma} = 0$ to $\dot{\gamma} = 0.05\tau^{-1}$ and Weissenberg number of $0 \leq We \leq 12$, according to the definition of the relaxation time of the polymers, discussed below.

The relaxation times of the polymers for different bending constants were estimated performing simula-

tions without liquid and at low grafting density ($\rho_g = 0.01\sigma^{-2}$). Studying the autocorrelation of the components of the end-to-end vector of the polymers it is possible to extract a characteristic correlation time of the chains:

$$C_i(t) = \frac{\langle (R_i(0) - \langle R_i \rangle) (R_i(t) - \langle R_i \rangle) \rangle}{\langle (R_i - \langle R_i \rangle)^2 \rangle}, \quad (10)$$

where $R_i(t)$ is the i -component of the end-to-end vector. Four values of the bending constant k_b were studied over a wide range of $k_B T$ values ($k_b/k_B T = 0; 1; 10$ and 100), giving the possibility to explore different rigidity regimes, from fully flexible chains ($k_b = 0\epsilon$), to very rigid rods that resemble pillars ($k_b = 80\epsilon$). For $k_b = 0\epsilon, 0.8\epsilon, 8\epsilon$ the correlation follows an exponential decay and the relaxation time can be obtained by fitting the curve $C(t) = \exp(-t/\tau_R)$. The relaxation of the polymers with $k_b = 80\epsilon$ is more complicated and does not follow a simple exponential decay. For short times, the behaviour is exponential, but it presents in addition a longtime correlation tail. This suggests complicated dynamics of the internal degrees of freedom of the molecule, excited by thermal fluctuations. In order to estimate a relaxation time in this case we fitted an exponential law up to a correlation value of $C(t) = 0.05$. This gives a relaxation time which is roughly the double of the short-time correlation decay ($\tau_R = 125\tau$).

Relaxation times of the grafted chains were also measured in simulations including the liquid. The results differ in less than 30% from those measured without liquid, except for the case of $k_b = 80\epsilon$. For the stiffest chains ($k_b = 80\epsilon$), we found that the collisions between liquid particles and the free end of the polymers decrease dramatically the relaxation time, turning out in a lower value than that of fully flexible chains. Taking this into account, it is evident that the relaxation times can be highly dependent on the particular system where the polymers are embedded. In order to obtain a characteristic polymer property, we decided to use the relaxation times calculated in absence of liquid, which are shown in Table I. We do not intend to study the complex dynamics of these highly rigid semiflexible polymers, but to estimate an order of magnitude of their relaxation times. A thorough study should be conducted to understand the relaxation kinetics of these semiflexible chains.

$k_b [\varepsilon]$	l_p/l_c	$l_p/\langle a \rangle$	$k_b/k_B T$	$\tau_R [\tau]$
0	0.16 ± 0.01	1.4 ± 0.1	0	17
0.8	0.22 ± 0.03	2.0 ± 0.3	1	18
8	1.12 ± 0.06	10.1 ± 0.5	10	50
80	10.1 ± 1.7	91 ± 15	100	260

Table I: Persistence length (l_p) over contour length (l_c) for every studied bending constant (k_b) studied. In the third column is presented the persistence length over mean bond length ($\langle a \rangle$). The persistence length covers a wide range of polymer rigidities, from fully flexible chains, to highly rigid rods. The values were obtained from independent simulations of isolated chains. The last column shows an estimate of the relaxation time of the grafted polymers, obtained from the correlation time of the end-to-end vector autocorrelation function.

In Table I the values for the bending constant are presented and compared to the energy of the typical thermal fluctuations. It is also shown, the persistence length l_p over the contour length of the chains l_c . We point out that both cases $l_p < l_c$ and $l_p > l_c$ are studied. For $k_b/k_B T \gg 1$ the relation $l_p \simeq k_b/k_B T$ holds [24]. To measure the persistence length, isolated chain simulations were performed under the same temperature and using the same interaction potentials as in the simulations for the brush-liquid system. The segment correlation $\cos(\theta_{|i-j|}) = \left\langle \frac{\mathbf{a}_i \cdot \mathbf{a}_j}{|\mathbf{a}_i| |\mathbf{a}_j|} \right\rangle$ is measured for long simulations (over 10^7 MD steps). Assuming an exponential decay of the bond correlation with the bond number, $\cos(\theta_s) = \exp(-s \cdot l_p / \langle |\mathbf{a}| \rangle)$, it is possible to estimate the persistence length l_p . For the stiffest cases $k_b = 8\varepsilon$ and $k_b = 80\varepsilon$, simulations with larger polymers ($N = 100$) were also carried out, to estimate more precisely l_p , yielding similar results as those obtained for $N = 10$.

III. RESULTS

A. Static properties

We begin our discussion by presenting the monomer density profiles of the system in equilibrium for all the studied bending constants k_b (see Figure 2). Upon increasing the rigidity of the bonds, the polymers stretch in the direction perpendicular to the grafted surface. This builds up the structure of the brush, noticeable in the sharp peaks of the polymer density profiles. The chemical incompatibility between liquid and polymer particles, expressed by the L-J parameters $\varepsilon_{pl} = 1/3\varepsilon_{ll} = 1/3\varepsilon_{pp}$, prevents the fluid from penetrating the brush in its liquid state. The liquid density decreases rapidly in the vicinity of the polymers, and only isolated particles enter in the brush, forming a gas in coexistence with the liquid. This gives rise to a well-defined, narrow liquid-brush interface, even for the lowest grafting density studied $\rho_g = 0.02\sigma^{-2}$.

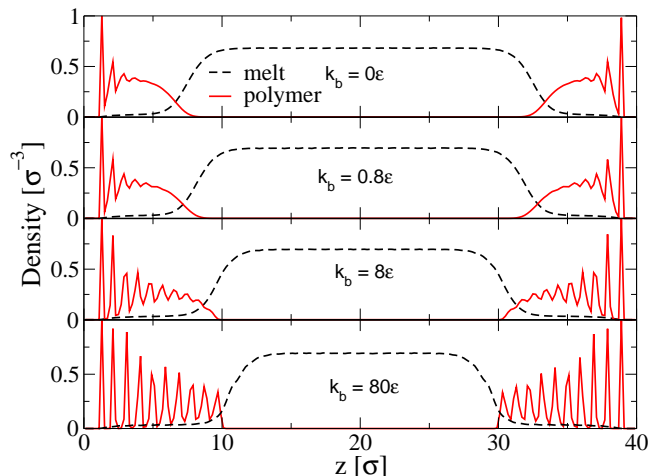


Figure 2: Density profiles for the liquid (dashed line) and the brush layer (red, continuous line) for the different bending constants. Upon increasing rigidity, the polymers stretch, and the structure of the brush is enhanced. The grafting density is $0.2\sigma^{-2}$ for all the cases.

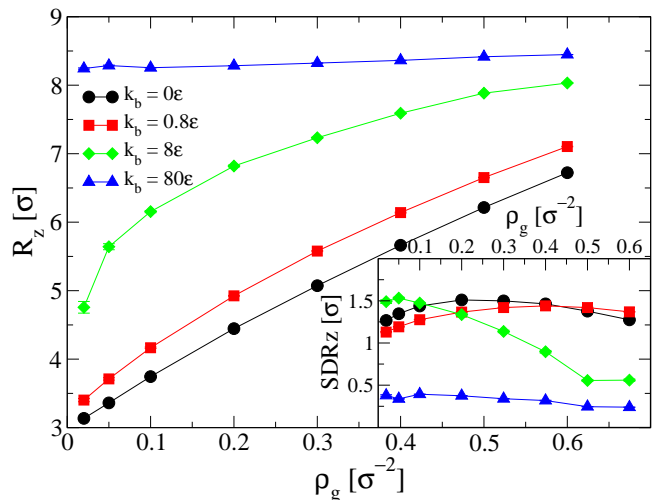


Figure 3: Perpendicular component of the polymer end to end vector R_z as a function of the grafting density ρ_g for the studied bending constants k_b . A linear relation may be observed between the brush height and the number of chains per surface area for the fully flexible case (black curve). The height of the stiffest chains ($k_b = 80$) is almost independent on the grafting density. Inset: Standard deviation of perpendicular component of the end-to-end vector, as a function of the grafting density. At low ρ_g the mobility of the semiflexible chains with $k_b = 8\varepsilon$ is higher than the mobility of fully flexible chains.

We note also that the fact the the liquid does not penetrate in the the brush agrees with the definition of the Cassie-Baxter state, present in nano-structured superhydrophobic surfaces[35, 58, 59]. This is illustrated for a relatively low grafting density $\rho_g = 0.05\sigma^{-2}$ in Fig. 1.

The height of the polymer brush varies significantly upon increase of the bending constant, due to the chain

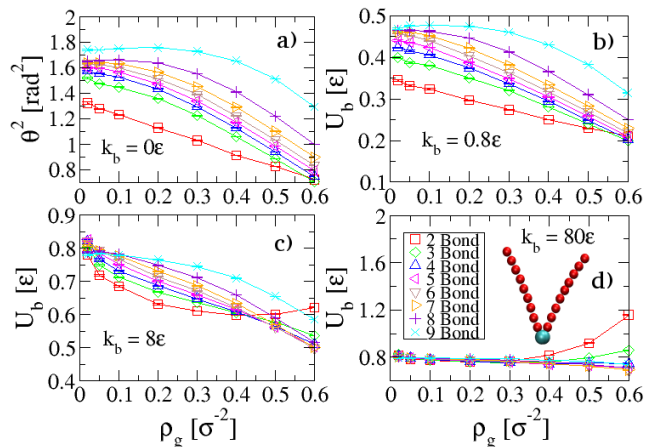


Figure 4: Panel (a): mean square bond angle of individual bonds versus grafting density (ρ_g). Panels (b)-(d): Bond energy (U_b) of individual bonds versus ρ_g . The first bond is not shown due to its special behavior (see text). The bond angles diminish upon increasing ρ_g , leading to an augment in the chains end to end distance. The energy also increases with the proximity of the bond to the free end bead. For $k_B = 80$ the bending energy per bond remains roughly the same for all grafting densities.

stretching. In Figure 3 the vertical component of the end-to-end vector (\mathbf{R}_{end}) is shown as a function of the grafting density for the different bending constants k_b . \mathbf{R}_{end} is defined as the vector joining both end-beads of the same polymer. As it was observed for the density profiles (Figure 2), increasing the bending rigidity results in a thicker brush. The behaviour is similar for all bending rigidities: the chains elongate in the z direction upon increasing ρ_g , due to excluded volume interactions, as reported in Refs. [18, 19] for brushes composed of fully flexible chains. This effect is less pronounced for the more rigid chains ($k_b = 8\epsilon$) and barely noticeable for the stiffest case ($k_b = 80\epsilon$), due to the finite extension reachable by the chains.

The inset of Figure 3 shows the standard deviation of R_z , SDR_z . This magnitude is associated with the typical chain height variation, i.e. the mobility of the end bead in z direction. Interestingly, there is a non-monotonic behaviour for the most flexible cases ($k_b = 0\epsilon$ and $k_b = 0.8\epsilon$). At low ρ_g , R_z increases with grafting density due to a larger free space available for the chains. Naturally, this causes an increase in SDR_z . At high ρ_g , the presence of neighbour polymers hinders the mobility of the end bead, decreasing SDR_z . The chains with $k_b = 8\epsilon$ have the greatest mobility at low ρ_g , but it decreases rapidly upon increasing ρ_g , because the bending potential allows global buckling of the chains, but no local bending. This means that the mobility of the end bead is highly dependent on the mobility of the entire polymer. SDR_z is fairly constant as function of ρ_g for the stiffest studied polymers ($k_b = 80\epsilon$).

To investigate the behavior of the internal degrees of

freedom of the polymers we measured the bond angles of each joint. Figure 4 shows the mean bending energy per bond $U_b = 1/2k_b \langle \theta_i^2 \rangle$ as a function of ρ_g , where θ_i is the angle formed by two consecutive bonds in the i -th joint. Naturally, θ decreases upon increasing the bending constant k_b , but this does not translate immediately in increment of U_b . At low ρ_g , increasing the bending constant from $k_b = 0.8\epsilon$ to $k_b = 8\epsilon$ roughly doubles the bending energy stored in each bond, but increasing the bending constant from $k_b = 8\epsilon$ to $k_b = 80\epsilon$ varies U_b in less than 5%. For the lowest grafting density, the increase in the end-to-end distance of the polymers with persistence length l_p is in good agreement with the Worm-like chain or Kratky-Porod model[60].

Upon increasing the grafting density, the excluded volume interactions induce polymer stretching (see Figure 3), which translates in a decrease in the bond angles. It can also be observed that bond angles near the free end-bead tend to be larger than those near the grafted end. Particularly, the last bead is only subject to the bending force of the last bond and is constantly colliding with liquid particles, which leads to a greater variance.

The first "orientation" bond (not shown in Figure 4) behaves differently than the other bond angles of the polymers, due to the constraints to which it is subjected to. For low bending constants ($k_b = 0\epsilon$ and $k_b = 0.8\epsilon$), the orientation angle is always lower than the chain bond angles, because the wall limits the values this angle can take. This reasoning is not true for the most rigid polymers ($k_b = 8\epsilon$ and $k_b = 80\epsilon$), because the strong bending forces bound the internal bond angles as well as the orientation bond, and the behaviour for both, internal and orientation angles, is similar at low ρ_g . At $\rho_g \geq 0.2\sigma^{-2}$ the presence of overlapping grafting points force the polymers to take high orientation angles as observed in the inset of Figure 4. This leads to a pronounced increase in the orientation bond energy, which comes only from the way in which the sample is generated. The grafting points are taken from a uniformly random distribution in the x - y plane and, consequently, the probability of producing a sample with overlapping grafting beads increases with grafting density.

B. Flow properties

The system was taken out of equilibrium by moving the walls at constant velocity in opposite directions[18, 22]. This induces a flow with a linear velocity profile in the liquid phase indicated in Figure 1. In Figure 5 the symmetrized velocity profile of the liquid is shown for various shear rates. In the bulk of the liquid, a linear dependence can be clearly observed, as expected for a simple liquid under these boundary conditions. In the vicinity of the interface (vertical dotted lines), the behaviour changes and near the wall the free gas particles match the wall velocity. It is interesting to note that the liquid layer in contact with the polymer brush does not match the wall

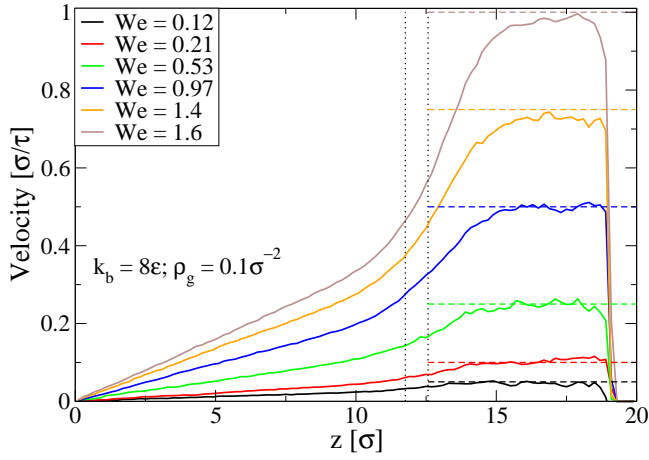


Figure 5: Velocity profiles as function of shear rates for a grafting density $\rho_g = 0.1\sigma^{-2}$ and bending constant $k_b = 8\varepsilon$. A linear profile can be observed in the bulk of the channel. In the vicinity of the brush-liquid interface (vertical dotted lines) there is a deviation from the linear dependence. The noisy section of the profile near the wall, corresponds to the fluid in its gaseous state. The wall velocity (and extension of the brush layer) is indicated with dashed horizontal lines.

velocity, i.e. the no-slip condition is violated and there is a partial slip of the liquid on the brush. The shear rate $\dot{\gamma}$ was obtained by fitting the linear velocity profile in the bulk of the liquid. $\dot{\gamma}$ increases with the wall velocity, but also depends on the grafting density ρ_g and the bending constant k_b . We define a Weissenberg number We , to quantify the shear rate with the natural relaxation of the semiflexible polymers. We is defined as the shear rate ($\dot{\gamma}$) times the relaxation time (τ_R) of an isolated chain at the same temperature than the simulated sample: $We = \dot{\gamma}\tau_R$. As shown in table I, the relaxation time is highly dependent on the bending constant.

At high grafting densities, the density profiles are almost independent of the shear velocity, while at low ρ_g , the brush height diminishes upon increasing shear rate. In Figure 6, the mean vertical component of the end to end vector (R_z), for the stiffest chains $k_b = 80\varepsilon$, is presented versus Weissenberg number We , for various grafting densities. A similar behaviour for R_z was observed as a function of We , for all the studied values of bending constants. The collisions with the liquid particles force the polymer chains to lean in the direction of the flow, thus decreasing their height. For the rod-like polymers ($k_b = 80\varepsilon$) there is also an increase in the mobility of the end bead in the direction perpendicular to the walls. To highlight this effect, the standard deviation of R_z is plotted as a function of We in the inset of Figure 6. For the lowest grafting density ($\rho_g = 0.02\sigma^{-2}$), SDR_z doubles its value when the shear rate is increased from $We = 0$ to $We = 10$. This effect was not observed for other bending constants ($k_b = 0\varepsilon, 0.8\varepsilon, 8\varepsilon$), because the mobility is less hindered by the bending rigidity. This data agrees with the model and simulations carried out

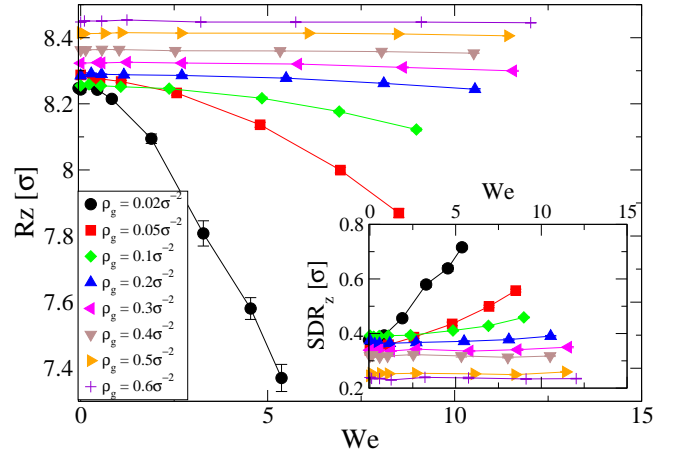


Figure 6: Perpendicular component of the end to end vector R_z for the polymer rods ($k_b = 80\varepsilon$) as a function of Weissenberg number for different grafting densities. For low ρ_g , the stretched polymers lean in the direction of the flow and the mean value of the normal component decreases. For high grafting the presence of near neighbour chains hinders the leaning of the polymers and this effect does not take place. Inset: Standard Deviation of R_z as a function of Weissenberg number. Upon increasing the shear rate, the mobility of the free end increases for low grafting densities. The rapidly flowing particles of the liquid collide with the polymer, bending it and increasing the standard deviation.

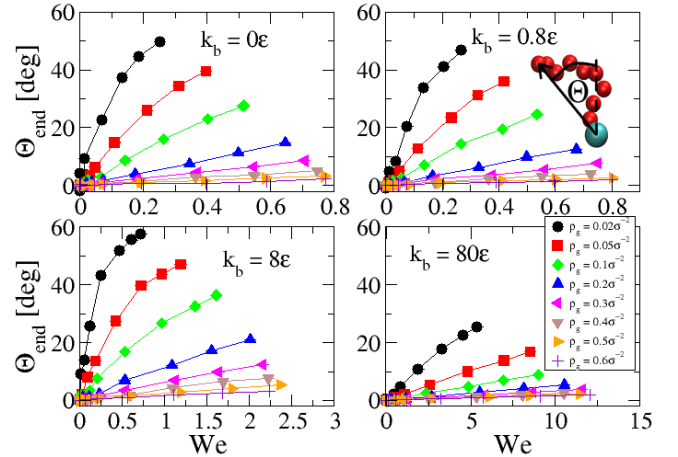


Figure 7: Mean end to end inclination angle of the chain (defined in the inset), as a function of the Weissenberg number for the studied grafting densities and bending constants. For lower grafting densities the polymers lean more, because there are less excluded volume interactions with other neighbours. Θ_{end} is greater for the chains with bending constant $k_b = 8\varepsilon$ than for the more flexible ones.

by Römer and Fedosov[28] in a similar system, but with hydrophilic brushes. The shear rates studied in our work correspond to $\dot{\gamma} \equiv \dot{\gamma}\eta l_c^3/k_B T$ in the range $0 \leq \dot{\gamma} \leq 40$.

In Figure 7 the end-to-end inclination angle (shown in the inset) is presented as a function of the Weissenberg number We for all the studied k_b and ρ_g . The inclina-

tion angle is calculated as $\Theta_{end} = \tan^{-1}(R_z/R_x)$, where R_x and R_z are the components of the end-to-end vector in the shear direction and perpendicular to the walls, respectively. Θ_{end} decreases upon increasing ρ_g , because excluded volume interactions among beads of neighboring chains hinder chain inclination. This is the same effect that causes the stretching of fully flexible chains in equilibrium[60]. As expected, increasing the shear rate induces a larger end-to-end angle, which means that the chains tilt in the direction of the flow. For $\rho_g \geq 0.2\sigma^{-2}$ the inclination angle is always lower than 20° , and the increment of Θ_{end} is linear with the shear rate. For lower grafting densities and high We , there is a non-linear behaviour, due to saturation effects. The dependence of Θ_{end} on the rigidity of the polymer is more complex. There are two different regimes according to the relation between persistence and contour lengths: a) $l_p < l_c$ and b) $l_p > l_c$. If the persistence length is lower than the contour length, increasing k_b (rigidity parameter) produces a higher end-to-end angle of the chains under shear. The consecutive bonds tend to stretch coherently in the shear direction, due to the correlation imposed by the bending potential. The pressure exerted by the simple liquid on the polymers induce chain buckling and they take a banana-like shape, maximizing Θ_{end} (see inset in Figure 7). Increasing k_b further (regime $l_p > l_c$) prevents the chain to achieve high local bending angles, and the polymer stretches in the vertical direction, disfavoring the buckling phenomenon. As seen in Figure 3, the stiffest chains $k_b = 80\varepsilon$ in equilibrium are totally stretched vertically for all ρ_g . It is important to recall that in this model there is a privileged orientation angle $\Theta_{end} = 0^\circ$, because the first bond θ_1 is subjected to the same bending potential as the rest of the polymer with an orientation perpendicular to the wall.

Another interesting quantity, is the standard deviation of the \mathbf{R}_{end} (SDR_x) component parallel to the shear direction. This magnitude gives information about the typical mobility of the polymer's free end-bead, around the mean value, in the shear direction. In Figure 8 is presented the dependence of SDR_x on ρ_g , for various shear rates and bending rigidities. It can be observed that for $l_p < l_c$ ($k_b \lesssim 8\varepsilon$), increasing bending rigidity induces a higher displacement of the free end. The pressure exerted by the liquid causes the more rigid polymers ($k_b = 8\varepsilon$) to bend in a defined direction, due to correlation between bonds, and thus enhances their displacement. Increasing k_b above $l_p \approx l_c$ hinders the mobility of the chain, because of the strong bending potential. This behaviour was previously observed by Milchev and Binder[61] for brushes in equilibrium without explicit solvent. An interesting feature of SDR_x is that for high $\dot{\gamma}$, the dependence on the grafting density is non-monotonic. At low ρ_g the chains lean in the shear direction and don't relax to the equilibrium configuration, thus having a small mobility. Increasing the number of neighbouring chains produces a screening effect, allowing the free end of the polymers to gain mobility. SDR_x reaches a maximum at interme-

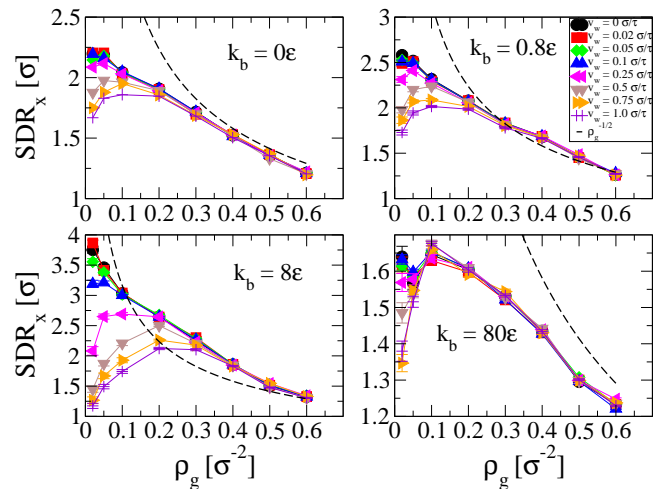


Figure 8: Standard deviation of the component parallel to the flow direction of the end to end vector (SDR_x) as a function of the grafting density (ρ_g) for the studied bending rigidities. The mean distance between grafting points is shown with a black dashed line. For low shear rates, the mobility of the polymers in the direction of the flow decreases monotonically with the grafting density. For high shear rates the behaviour of SDR_x is non monotonic with ρ_g . At low grafting densities and large shear rates, the chains lean in the direction of the flow and are not able to relax to the equilibrium configuration, due to collisions with liquid particles. Upon increasing the number of chains per surface area, there is a screening effect that allows polymers to gain mobility in the shear direction. This effect has a peak at intermediate ρ_g , decreasing then for higher grafting due to the hindering of the mobility by excluded volume interactions.

diated ρ_g , because at high grafting densities the mobility of the free end decreases, due to excluded volume interactions.

The typical displacement SDR_x is compared to the mean distance between grafting points (dashed line in Figure 8). As expected for high ρ_g , the chain movement is limited by the presence of neighbour polymers, and SDR_x match the mean distance between neighbours. At low grafting densities, the standard deviation of R_x is limited by the finite length of the polymer, and by entropic effects. At intermediate ρ_g , SDR_x is higher than the mean distance between grafting points for semiflexible chains ($k_b = 0.8\varepsilon$ and $k_b = 8\varepsilon$). It may be also observed that for rigid rods ($k_b = 80\varepsilon$) SDR_x is always less than the mean distance between grafting points. This indicates that even for high ρ_g , the dynamics of this polymers are greatly affected by the bending force.

We also checked the existence of cyclic motion dynamics in semiflexible chains under shear, found in previous works for fully flexible isolated grafted chains and polymer brushes[20, 22]. We analysed the effect of stiffness in the mechanism of cyclic motion, whose origin is attributed to spontaneous fluctuations of the polymer chains towards regions of higher velocity in the liquid. According to this description, a stiffer chain should have

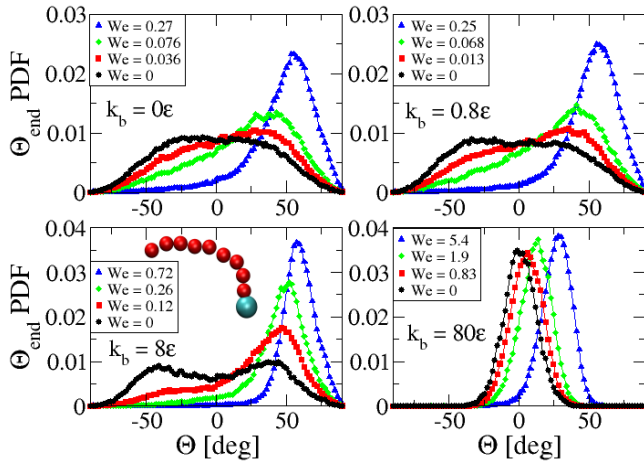


Figure 9: Probability density function (PDF) of the end-to-end angle of the polymers as a function of shear rate, for the lowest grafting density $\rho_g = 0.02\sigma^{-2}$. For $k_b = 8\epsilon$, the equilibrium PDF is bimodal. The pressure exerted by the liquid difficults the full stretching of polymers perpendicular to the wall, giving rise to a non vanishing end-to-end angle.

a reduction in the cyclic motion, because the thermal fluctuations are reduced. This is in fact what we observe. We computed the mean brush momentum velocity profile $p(z) = \langle m\rho(z)v(z) \rangle$, exactly in the same way, than previous references[22] (not shown). The presence of cyclic motion is evidenced when a positive $p(z)$ is observed in the region in which the chains are directly exposed to and dragged by the fluid and, at the same time, a negative $p(z)$ is observed in an inner region, inside the brush. We found cyclic motion dynamics for bending constants $k_b = 0.8\epsilon$ and $k_b = 8\epsilon$. This was the case for low grafting density ($\rho_g = 0.02\sigma^{-2}$ and $0.05\sigma^{-2}$), in which the dynamics of chains can be regarded as independent, but also for higher grafting ($\rho_g = 0.3\sigma^{-2}$) already in the brush regime. The cyclic dynamics is indeed reduced upon increase of the chain stiffness and vanishes completely for the stiffest chains ($k_b = 80\epsilon$). A more comprehensive characterization of the effect and its consequences for flow inversion[20, 22] could be an interesting future study.

In Figure 9 the probability density function (PDF) of the end to end inclination angle Θ_{end} is presented for various Weissenberg numbers and bending rigidities. The equilibrium distribution has mean value $\langle \Theta_{end} \rangle = 0$ for all cases, and high variance $var(\Theta_{end}) = \langle \Theta_{end}^2 \rangle - \langle \Theta_{end} \rangle^2$. Upon increasing the shear rate, the chains lean in the flow direction and decrease their mobility, thus raising the mean value and reducing the variance. The shape of PDF(Θ_{end}) is highly non-symmetrical with respect to the maximum for the samples under shear. This behaviour is observable for all bending rigidities, except for $k_b = 80\epsilon$ that is less noticeable. It is interesting to note that all the PDF deviate from a normal distribution, and particularly the tails follow a non-gaussian decay. This non-gaussian behaviour was already found in

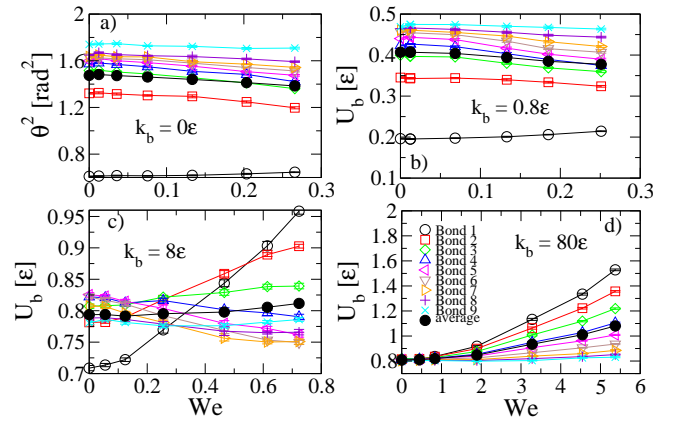


Figure 10: Panel (a): Mean square angle of each bond in the chain as function of Weissenberg number (We) for the fully flexible case and $\rho_g = 0.02\sigma^{-2}$. Panels (b)-(d): Bond bending energy $U_b = 1/2 \cdot k_b \cdot \theta^2$ of each bond as function of We and $\rho_g = 0.02\sigma^{-2}$. For the most flexible polymers studied ($k_b = 0$ and $k_b = 0.8$), the bonds in the chain decrease with increasing shear rate, and the chains end-to-end distance increases. The orientation angle (Bond 1) increases because the chains lean on the direction of the flowing liquid in the channel. The behaviour of the rods ($k_b = 80$) is different: all the bond angles increase upon rising the shear rate.

theory and experiments of single chains under shear.[62]

The buckling process for the case $k_b = 8\epsilon$ can also be observed from the equilibrium PDF (black circles, in lower left panel in Fig. 9). There are two maxima, which correspond to $\Theta_{end} = \pm 40^\circ$, and there is a local minimum at $\Theta_{end} = 0$, which corresponds to the free-end of the polymer, vertically aligned with the grafted monomer. The pressure exerted by the liquid induces a buckling in the semiflexible chains, adopting the shape shown in the inset of Fig. 9. This effect is most noticeable for chains whose persistence length is similar to the contour length, due to the global order these polymers achieve. For lower bending, a flat plateau at the maximum, more than a bimodal distribution is observed. While for high bending rigidity ($k_b = 80\epsilon$), the equilibrium distribution corresponds clearly to a normal curve.

It's interesting to analyze how the internal degrees of freedom of the polymers are affected by the shear stress. In Figure 10 is presented the bending energy U_b for each bond as a function of the Weissenberg number We , for the lowest grafting density ($\rho_g = 0.02\sigma^{-2}$). Two different regimes can be distinguished: for $l_p \ll l_c$ (panels a and b) the orientation angle (Bond 1) is considerable smaller than the internal angles, and the angles decrease upon increasing shear rate, thus increasing the end to end distance. In this case, the total bending energy is reduced with increasing shear rate. For $l_p \gg l_c$ (panel d), the orientation angle is greater than the internal angles, and the bending energy of all bonds increase upon increasing We . It is also observed a decrease in the distance between grafted and end beads. In this regime, the chains tend to take a banana-like shape, leaning with the flowing

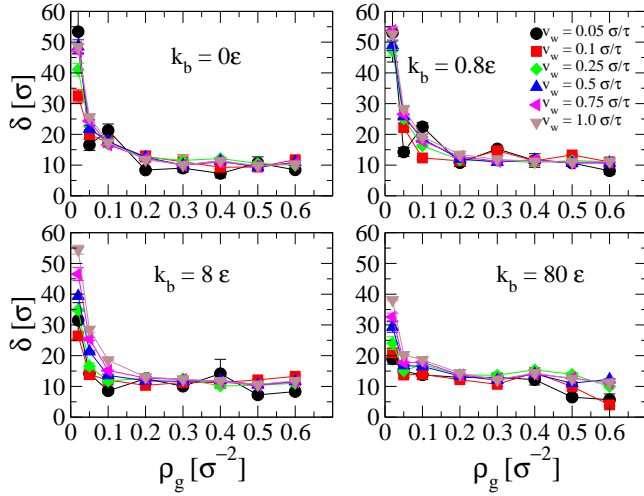


Figure 11: Slip length (δ) as a function of the grafting density (ρ_g) for the studied shear rates. The slip length decreases rapidly upon increasing ρ_g . For intermediate and high grafting densities ($\rho_g \geq 0.1\sigma^{-2}$) δ takes roughly the same value $\delta \approx 11\sigma$ for every wall velocity and bending rigidity. All the studied cases present non-zero slip length, indicating that the no-slip condition between the polymer brush and the free melt does not hold. The rod-like polymers ($k_b = 80\epsilon$) are the ones that offer the most resistance to the liquid flow for every grafting density and shear rate.

liquid, and decreasing the end to end distance.

Polymers of $k_b = 8\epsilon$ are a limit case (panel c), because the persistence length coincides with the contour length. The average Bending energy (solid black dots in Fig. 10) and the end-to-end distance (not shown) changes less than 2%. In this limiting case, there are no important changes in the internal structure of the polymers, which implies that the external perturbation only alters the inclination angle. In addition, it can be observed that the variation of bending energy between internal angles of the same chain do not vary more than 30% for $We \leq 4$. This means that the contribution of the internal angles to the total inclination of the chain is roughly equidistributed along the polymer, as already observed by Milchev and Binder[61].

As mentioned above, the no-slip condition was violated in every system studied. The friction reduction in systems with polymer brushes has been a well known interesting feature for over a decade now[4]. We quantify here the effects of stiffness in the semiflexible polymers. To quantify this phenomenon, the slip length (δ) was measured and plotted versus the grafting density ρ_g in Figure 11. δ is defined as the distance at which the extrapolation of the far field velocity profile of the liquid matches the substrate velocity (see Ref. [59]). The liquid-polymer interface position was defined as the z coordinate at which the function $f(z) = \rho_l(z) \cdot \rho_p(z)$ presents a maximum, where ρ_l is the liquid density, ρ_p is the polymer density and z is the coordinate perpendicular to the walls. At low ρ_g , the slip of liquid over the polymer brush is highly de-

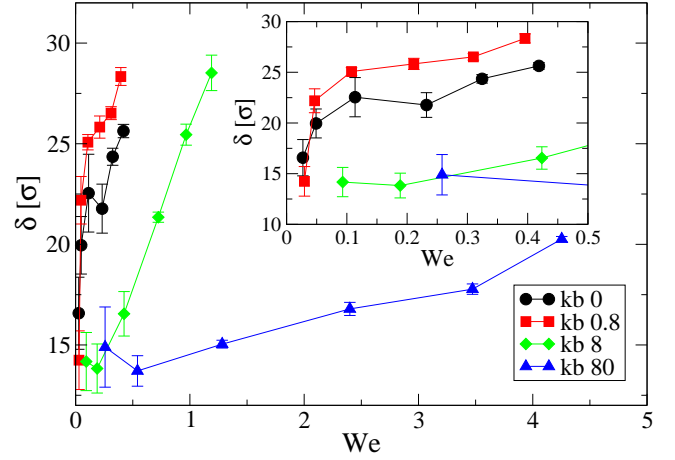


Figure 12: Slip length δ as a function of Weissenberg number We , for systems with low grafting density ($\rho_g = 0.05\sigma^{-2}$). The slip length is highly dependent on the bending constant at lower grafting densities. The stiffest chains ($k_b = 80\epsilon$) present less slip for all shear rates studied. It is interesting to note the non-monotonic dependence of δ with the bending constant k_b . Inset: detail of δ at low We . The slip is higher for the semiflexible polymers with $k_b = 0.8\epsilon$, than for the fully flexible polymers.

pendent on the properties of the substrate. Varying the number of grafted polymers per surface area and their rigidity yield different results. In general, δ decreases rapidly upon increasing grafting density, but the dependence with the stiffness (k_b) is non-monotonic. At intermediate to high grafting densities ($\rho_g > 0.1\sigma^{-2}$), δ seems to saturate and takes a constant value, regardless of the flexibility parameter k_b , the shear rate ($\dot{\gamma}$), or the grafting density. Only for rigid rods ($k_b = 80\epsilon$), there is a decrease in the slip at high grafting densities, and $We \lesssim 1$. We think that above $\rho_g = 0.1\sigma^{-2}$, the slip length is determined strongly by the brush-liquid compatibility which was fixed in this study with the values $\epsilon_{lp} = 1/3\epsilon_{ll} = 1/3\epsilon_{pp}$.

In Figure 12 is presented the slip length δ as a function of the Weissenberg number We , for a low grafting density $\rho_g = 0.05\sigma^{-2}$. For every bending constant, δ increases upon increasing shear rate, at low grafting densities, as it was already reported for fully flexible chains[18]. A very interesting feature is that semiflexible chains with $k_b = 0.8\epsilon$ ($l_p/l_c \simeq 0.2$) induce higher slip length than fully flexible chains, for all the studied shear rates. We think that a moderate stiffness in the polymer could reduce the contacts of the chains with the liquid as compared to the case of fully flexible chains in mushroom regime. The dependence of δ on k_b is non-monotonic. Increasing further the stiffness (from $k_b = 0.8\epsilon$ to $k_b = 8\epsilon$) decreases the slip length. Even though the slip for $k_b = 8\epsilon$ is smaller than the slip of the more flexible chains, the rate of change of δ with We is roughly the same for $We \geq 0.5$. The rigid-rods brush ($k_b = 80\epsilon$) is harder, and it shows a greater capacity

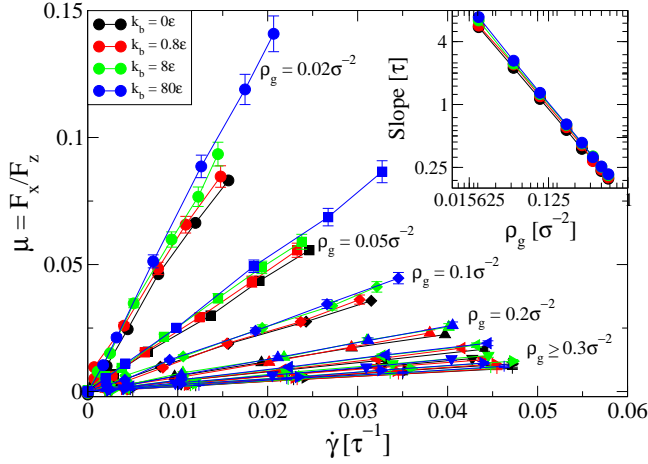


Figure 13: Friction coefficient μ of the system versus shear rate. Each group of curves corresponds to a different grafting density ρ_g . It can be observed that μ is proportional to the shear rate, and the slope is highly dependent on the grafting density ρ_g . For systems with the same ρ_g , the friction coefficient is higher, the higher the bending constant. Inset: double-logarithmic scaling plot for the slope of μ vs $\dot{\gamma}$, as a function of the grafting density. The dependence of the slope on ρ_g seems to follow a power law.

to drag liquid along, than the more flexible brushes. It has lower slip lengths in the whole range of We studied, and the growing slope is also lower. It is known that the slip length is highly dependent on the normal pressure: the higher the pressure, the smaller the slip[59]. In this case, the normal pressure of the different systems varied less than 15%, and decreased monotonically with the bending constant. This implies that the non-monotonic dependence of the slip length on the bending constant can not be attributed only to variations in the normal pressure.

The force applied to the system in the direction of the wall displacement as a function of the shear rate was also analyzed. The data from the eight different grafting densities, four bending constants, and five shear rate values collapse to a single straight line (not shown). This means that the relation between the total force exerted on the walls and the shear rate is independent of the polymer brush, and only depends on the liquid. It was possible to extract the viscosity of the simple liquid from the relation: $F_x = \eta \cdot A \cdot \dot{\gamma}$, obtaining a value of $\eta = 1.28\epsilon\tau\sigma^{-3}$ [18, 21]. This essentially shows that the liquid behaves as a simple (newtonian) liquid with a well defined viscosity for the whole range of shear rates, and that the different morphologies of brush-liquid interface or gas content inside the brush layer does not have a significative role in the diffusion of momenta in the system.

Another useful quantity to compare different polymer brushes is the kinetic friction coefficient (μ), defined as the quotient between shear and normal forces: $\mu = F_x/F_z$. Figure 13 presents μ versus $\dot{\gamma}$ as a function of the bending constant k_b , for different grafting densities

ρ_g . It may be observed that the friction coefficient does not depend strongly on the stiffness of polymer chains. The variation of μ between systems with the same grafting density and under the same shear rate is in all cases less than 20%. Upon increasing the grafting density, the friction coefficient decreases. As encountered in other studies [14, 21], μ increases with shear rate. In this case it is observed that the relation between μ and $\dot{\gamma}$ is linear for high ρ_g , because the normal force variation is very small with shear rate for intermediate to high grafting densities.

Every curve was fitted, performing a linear regression of the form $\mu = m\dot{\gamma}$, with only one parameter (m). The slope (m) of each curve is plotted against ρ_g in the inset of Figure 13, in a log-log scale. This implies that m follows a power law of the form $m = B(k_b)\rho_g^{-1}$, where $B(k_b)$ is a function that depends on k_b only. The exponent of ρ_g turns out to be -1 for all the bending rigidities. Combining the last two equations is possible to obtain a scaling law for the behaviour of the friction coefficient μ as a function of the shear rate $\dot{\gamma}$ and the grafting density ρ_g :

$$\mu \sim B(k_b)\dot{\gamma}\rho_g^{-1} \quad (11)$$

It is interesting to note that the friction coefficient decreases with increasing number of grafted chains per surface area. We think that increasing ρ_g hinders the liquid from penetrating the polymer brush. Adding polymer chains in this superhydrophobic system could result in a smoother liquid-brush interface, thus decreasing μ . The components of the total force (F_x and F_z) acting on the grafted end of the polymers have a different dependence on the grafting density (not shown). While F_z increases linearly with ρ_g , F_x increases rapidly at low ρ_g , and at high grafting densities ($\rho_g > 0.3\sigma^{-2}$) seems to reach a saturation value. We note however, that friction phenomena are frequently scale dependent and friction coefficients give different results in experimental measurements at nanoscopic and macroscopic levels[63]. They have usually contributions from dissipative processes at various length scales. Also, macroscopic concepts are not readily extrapolated down to small scale topographies[59].

IV. CONCLUSIONS

In this work, we studied comprehensively the properties in equilibrium and under flow, of an interface of grafted semiflexible chains and a simple liquid. We chose the interaction parameters between liquid and polymer chains such that the liquid is in super-hydrophobic regime on the top of the brush in the well-known Cassie-Baxter state. In such, the liquid does not wet the interior of the grafted layer of polymers and only molecules belonging to the coexisting gas phase enter in the grafted polymer layer. The grafting density was varied in a wide

range, from mushroom regime of mostly isolated chains to a dense brush with significant excluded volume interactions among chains. Also the stiffness of the chains were studied in an ample physical range, from fully-flexible chains to highly rigid chains, in which the polymers resemble pillars, which were used as structures to produce super-hydrophobic surfaces. We characterized the properties of the chains by independent simulations in which we calculate the persistence length, and the relaxation dynamics, by means of the time correlation function of the end-to-end vector.

We analysed the equilibrium structure of the grafted polymer layers with density profiles, the behavior of the end-to-end vector components, mean angles with the grafting plane, and bending energy of the chains. The mean bending energy per bond behaves in a non-trivial way, while for low bending constants ($k_b \sim k_B T$) the energy increases with stiffness, for high k_b it reaches a saturation value. We studied also the probability density function of these angles in equilibrium and under flow, obtaining non-gaussian distributions. We found a rich and distinctive behavior of the chains for different bending rigidities. This is also reflected in the typical shape that the chains adopt while supporting the liquid layer on top of them. The most flexible polymers assume a typical mushroom configuration for low grafting densities. For bending constants corresponding to persistence lengths of the order of the chains' contour length, the polymers bend in a banana-like shape to balance the pressure exerted by the liquid. This leads to a higher displacement of the end-to-end vector in the direction parallel to the substrate. In the rigid rod limit, the polymers adopt typically a strait vertical configuration, and buckling phe-

nomenon is observed, due to the normal force exerted by the liquid. By moving the confining walls at constant opposite velocities, we generate a linear Couette flow in the liquid and studied the behavior of the brush layer under flow as function of grafting density and shear rates. We measured the slip length of the liquid and found a saturation to a well defined value upon increasing grafting densities. At low grafting, where excluded volume effects are negligible and the behavior is dominated by the properties of isolated chains, we found that a moderate stiffness produces higher slip than fully flexible chains. For even stiffer chains, the slip is reduced, giving rise to a very interesting non-monotonic behavior of slip lengths and velocities as a function of chain rigidity. We measured also the friction coefficient of the interface by means of the mean normal and shear forces, needed to impose a given shear rate. For a given shear rate, we found that friction is inversely proportional to grafting density. It could be interesting to expand these studies analysing the differences in the reported behavior for liquids of lower chemical incompatibility with the brush chains and the dynamics of droplets on top of these polymer-coated surfaces of semiflexible chains. This should be also of relevance for the fields of super-hydrophobic responsive surfaces and microfluidics.

Acknowledgments

Financial support through grants PICT-2011-1887, PIP 2011, INN-CNEA 2011, PICT-E 2014, is gratefully acknowledged. We thank also Marcus Müller for fruitful discussions about different aspects of the present work.

-
- [1] R. Advincula, *Polymer brushes synthesis, characterization, applications*, Wiley-VCH, Weinheim, 2004.
 - [2] R. Barbey, L. Lavanant, D. Paripovic, N. Schüwer, C. Sugnaux, S. Tugulu and H.-A. Klok, *Chemical Reviews*, 2009, **109**, 5437–5527.
 - [3] O. Azzaroni, *Journal of Polymer Science Part A: Polymer Chemistry*, 2012, **50**, 3225–3258.
 - [4] J. Klein, E. Kumacheva, D. Mahalu, D. Perahia and L. J. Fetters, *Nature*, 1994, **370**, 634–636.
 - [5] E. Stratakis, A. Mateescu, M. Barberoglou, M. Vamvakaki, C. Fotakis and S. H. Anastasiadis, *Chem. Commun.*, 2010, **46**, 4136–4138.
 - [6] S. Peng and B. Bhushan, *RSC Adv.*, 2012, **2**, 8557–8578.
 - [7] T. Chen, R. Ferris, J. Zhang, R. Ducker and S. Zauscher, *Progress in Polymer Science*, 2010, **35**, 94 – 112.
 - [8] K. Binder and A. Milchev, *Journal of Polymer Science Part B: Polymer Physics*, 2012, **50**, 1515–1555.
 - [9] S. Weinbaum, J. M. Tarbell and E. R. Damiano, *Annu Rev Biomed Eng.*, 2007, **9**, 121–67.
 - [10] M. Deng, X. Li, H. Liang, B. Caswell and G. E. Karniadakis, *Journal of Fluid Mechanics*, 2012, **711**, 192–211.
 - [11] K. Binder, T. Kreer and A. Milchev, *Soft Matter*, 2011, **7**, 7159–7172.
 - [12] T. Lee, E. Charrault and C. Neto, *Advances in Colloid and Interface Science*, 2014, –.
 - [13] S. T. Milner, *Science*, 1991, **251**, 905–914.
 - [14] A. Galuschko, L. Spirin, T. Kreer, A. Johner, C. Pastorino, J. Wittmer and J. Baschnagel, *Langmuir*, 2010, **26**, 6418–6429.
 - [15] T. Kreer, M. H. Müser and K. Binder, *Comp. Phys. Comm.*, 2002, **147**, 358.
 - [16] T. Kreer, M. H. Müser, K. Binder and J. Klein, *Langmuir*, 2001, **17**, 7804–7813.
 - [17] G. S. Grest, *Adv. Polym. Sci.*, 1999, **138**, 149–183.
 - [18] C. Pastorino, K. Binder, T. Kreer and M. Müller, *J. Chem. Phys.*, 2006, **124**, 064902.
 - [19] C. Pastorino, K. Binder and M. Müller, *Macromolecules*, 2009, **42**, 401–410.
 - [20] M. Müller and C. Pastorino, *Europhys. Lett.*, 2008, **81**, 28002.
 - [21] A. G. Goicochea, E. Mayoral, J. Klapp and C. Pastorino, *Soft Matter*, 2014, 166–174.
 - [22] C. Pastorino and M. Müller, *The Journal of Chemical Physics*, 2014, **140**, 166–174.
 - [23] A. Milchev and K. Binder, *The Journal of Chemical Physics*, 2012, **136**, 194901.

- [24] A. Milchev and K. Binder, *EPL (Europhysics Letters)*, 2013, **102**, 58003.
- [25] F. Goujon, P. Malfreyt and D. J. Tildesley, *ChemPhysChem*, 2004, **5**, 457–464.
- [26] P. Benetatos, E. M. Terentjev and A. Zippelius, *Phys. Rev. E*, 2013, **88**, 042601.
- [27] Y. W. Kim, V. Lobaskin, C. Gutsche, F. Kremer, P. Pincus and R. R. Netz, *Macromolecules*, 2009, **42**, 3650–3655.
- [28] F. Römer and D. A. Fedosov, *EPL (Europhysics Letters)*, 2015, **109**, 68001.
- [29] Y. W. Kim and R. R. Netz, *Phys. Rev. Lett.*, 2006, **96**, 158101.
- [30] J. Elgeti and G. Gompper, *Proceedings of the National Academy of Sciences*, 2013, **110**, 4470–4475.
- [31] P. Roach, N. F. Shirtcliffe and M. I. Newton, *Soft Matter*, 2008, **4**, 224.
- [32] Y.-L. Zhang, H. Xia, E. Kim and H.-B. Sun, *Soft Matter*, 2012, **8**, 11217–11231.
- [33] J. Genzer and K. Efimenko, *Science*, 2000, **290**, 2130–2133.
- [34] R. N. Wenzel, *Ind. Eng. Chem.*, 1936, **28**, 988–994.
- [35] A. B. D. Cassie and S. Baxter, *Trans. Faraday Soc.*, 1944, **40**, 546–551.
- [36] G. D. Bixler and B. Bhushan, *Soft Matter*, 2012, **8**, 11271–11284.
- [37] F. Shi, J. Niu, J. Liu, F. Liu, Z. Wang, X.-Q. Feng and X. Zhang, *Advanced Materials*, 2007, **19**, 2257–2261.
- [38] C.-H. Choi and C.-J. Kim, *Phys. Rev. Lett.*, 2006, **96**, 066001.
- [39] N. J. Shirtcliffe, G. McHale, M. I. Newton and Y. Zhang, *ACS Applied Materials & Interfaces*, 2009, **1**, 1316–1323.
- [40] R. Truesdell, A. Mammoli, P. Vorobieff, F. van Swol and C. J. Brinker, *Phys. Rev. Lett.*, 2006, **97**, 044504.
- [41] A. Poynor, L. Hong, I. K. Robinson, S. Granick, Z. Zhang and P. A. Fenter, *Phys. Rev. Lett.*, 2006, **97**, 266101.
- [42] D. C. Tretheway and C. D. Meinhardt, *Physics of Fluids (1994-present)*, 2004, **16**, 1509–1515.
- [43] D. M. Huang, C. Sendner, D. Horinek, R. R. Netz and L. Bocquet, *Phys. Rev. Lett.*, 2008, **101**, 226101.
- [44] K. Kremer and G. S. Grest, *The Journal of Chemical Physics*, 1990, **92**, 5057–5086.
- [45] G. S. Grest and K. Kremer, *Phys. Rev. A*, 1986, **33**, 3628–3631.
- [46] J.-L. Barrat and L. Bocquet, *Phys. Rev. Lett.*, 1999, **82**, 4671–4674.
- [47] F. Ould-Kaddour and D. Levesque, *The Journal of Chemical Physics*, 2011, **135**, –.
- [48] S. M. Dammer and D. Lohse, *Phys. Rev. Lett.*, 2006, **96**, 206101.
- [49] F. Léonforte, J. Servantie, C. Pastorino and M. Müller, *Journal of Physics: Condensed Matter*, 2011, **23**, 184105.
- [50] P. J. Hoogerbrugge and J. M. V. Koelman, *Europhys. Lett.*, 1992, **19**, 155.
- [51] R. D. Groot and P. B. Warren, *J. Chem. Phys.*, 1997, **107**, 4423–4435.
- [52] P. Español, *Phys. Rev. E*, 1995, **52**, 1734–1742.
- [53] T. Soddemann, B. Dünweg and K. Kremer, *Phys. Rev. E*, 2003, **68**, 046702.
- [54] C. Pastorino and A. Goicochea, in *Selected Topics of Computational and Experimental Fluid Mechanics*, ed. J. Klapp, G. Ruíz Chavarría, A. Medina Ovando, A. López Villa and L. D. G. Sigalotti, Springer International Publishing, 2015, pp. 51–79.
- [55] C. Pastorino, T. Kreer, M. Müller and K. Binder, *Phys. Rev. E*, 2007, **76**, 026706.
- [56] D. Frenkel and B. Smit, *Understanding Molecular Simulation, 2nd Edition*, Academic Press, San Diego, 2002.
- [57] M. Müller and L. G. MacDowell, *Macromolecules*, 2000, **33**, 3902–3923.
- [58] B. Wang, Y. Zhang, L. Shi, J. Li and Z. Guo, *J. Mater. Chem.*, 2012, **22**, 20112–20127.
- [59] N. Tretyakov and M. Müller, *Soft Matter*, 2013, **9**, 3613–3623.
- [60] M. Rubinstein and R. H. Colby, *Polymer Physics*, Oxford, 2003.
- [61] A. Milchev and K. Binder, *Soft Matter*, 2014, **10**, 3783–3797.
- [62] R. G. Winkler, *Phys. Rev. Lett.*, 2006, **97**, 128301.
- [63] M. Nosonovsky and B. Bhushan, *Materials Science and Engineering: R: Reports*, 2007, **58**, 162 – 193.